Yan, Chengzhan; Zhao, Huaping; Li, Jun; Jin, Huile; Liu, Long; Wu, Wanyi;
Wang, Jichang; Lei, Yong; Wang, Shun:

Mild-temperature solution-assisted encapsulation of phosphorus into ZIF-8 derived porous carbon as lithium-ion battery anode

Original published in:	Small. - Weinheim : Wiley-VCH. - 16 (2020), 11, art. 1907141, 7 pp.
Original published:	2020-02-21
ISSN:	1613-6829
DOI:	10.1002/smll.201907141
[*Visited:*	2020-05-15]

NANO · MICRO small
www.small-journal.com

Mild-Temperature Solution-Assisted Encapsulation of Phosphorus into ZIF-8 Derived Porous Carbon as Lithium-Ion Battery Anode

Chengzhan Yan, Huaping Zhao, Jun Li, Huile Jin, Long Liu, Wanyi Wu, Jichang Wang, Yong Lei, and Shun Wang**

The high theoretical capacity of red phosphorus (RP) makes it a promising anode material for lithium-ion batteries. However, the large volume change of RP during charging/discharging imposes an adverse effect on the cyclability and the rate performance suffers from its low conductivity. Herein, a facile solution-based strategy is exploited to incorporate phosphorus into the pores of zeolitic imidazole framework (ZIF-8) derived carbon hosts under a mild temperature. With this method, the blocky RP is etched into the form of polyphosphides anions (PP, mainly P_5^-) so that it can easily diffuse into the pores of porous carbon hosts. Especially, the indelible crystalline surface phosphorus can be effectively avoided, which usually generates in the conventional vapor-condensation encapsulation method. Moreover, highly-conductive ZIF-8 derived carbon hosts with any pore smaller than 3 nm are efficient for loading PP and these pores can alleviate the volume change well. Finally, the composite of phosphorus encapsulated into ZIF-8 derived porous carbon exhibits a significantly improved electrochemical performance as lithium-ion battery anode with a high capacity of 786 mAh g^{-1} after 100 cycles at 0.1 A g^{-1}, a good stability within 700 cycles at 1 A g^{-1}, and an excellent rate performance.

Red phosphorus (RP), as a promising anode material for lithium-ion batteries (LIBs), can theoretically deliver 2596 mAh g^{-1} capacity with a redox potential of 0.8–1.2 V.[1–4] Unfortunately, RP suffers from two major deficiencies, the low electrical conductivity (10^{-12} S m^{-1}) and the large volume change (>300%) during charging/discharging. Particularly, the huge volume change of RP is going to create massive gaps among the originally dense electrode, resulting in a breaking-off effect, so-called "micro-breaking".[5] The breaking-off effect will give rise to severe capacity decay and poor cycling stability. To address the aforementioned two challenging issues, extensive studies have suggested that the encapsulation of RP into porous carbon hosts is an efficient approach, in which porous carbon hosts not only offers a "conductive network" to improve the overall conductivity of the electrode but also serves as "limited carrier" of the loaded RP to buffer its volume change during the intercalation/deintercalation processes and finally alleviate the breaking-off effect to improve the lifespan.

Up to now, several synthesis techniques have been developed to introduce RP into carbon hosts. A general strategy is to physically deposit RP in the carbon hosts via an evaporation/condensation process.[5–19] Note that a necessary high temperature of 500–900 °C is commonly applied in order to ensure the conversion of the bulk RP into the gas phase. In this process, RP sublimates and diffuses in the carbon hosts and finally form a carbon/RP composite. The internal cavity of carbon hosts will accommodate the volume expansion of RP. With respect to carbon hosts, multi-walled carbon nanotubes (MWCNTs) have been mostly investigated as one example. It has been revealed that the main shortcoming of the evaporation/condensation method is the inevitable condensation of amorphous and crystalline RP on the outer wall from the sublimated RP nanoparticles besides inside MWCNTs.[5,6] Crystalline RP anchored on the outer wall of MWCNTs is usually too stable to be removed with common solvents such as distilled water, ethanol, and carbon disulfide (CS_2) or even by subsequent annealing,[5,6] and consequently imposes an adverse effect on the cyclability.[5] Moreover, the unstable, toxic, and flammable white phosphorus will also generate accompanied with the evaporation/condensation process, generally requiring further annealing thereafter washing with toxic CS_2.[5–19] Recently, a solution-processed encapsulation method has been developed to facilitate the formation of RP nanoparticles inside MWCNTs and meanwhile allow the easy removal of the external phosphorus anchored on

C. Yan, Dr. J. Li, Prof. H. Jin, W. Wu, Prof. S. Wang
Key Laboratory of Carbon Materials of Zhejiang Province
Institute of New Materials and Industrial Technologies
College of Chemistry and Materials Engineering
Wenzhou University
Wenzhou, Zhejiang 325035, China
E-mail: shunwang@wzu.edu.cn
Dr. H. Zhao, L. Liu, Prof. Y. Lei
Institute of Physics and IMN MacroNano
Ilmenau University of Technology
Ilmenau 98693, Germany
E-mail: yong.lei@tu-ilmenau.de
Dr. J. Li, Prof. J. Wang
Department of Chemistry and Biochemistry
University of Windsor
Windsor, ON N9B3P4, Canada
The ORCID identification number(s) for the author(s) of this article can be found under https://doi.org/10.1002/smll.201907141.

DOI: 10.1002/smll.201907141

the outer wall of MWCNTs because this solution-based process avoids the formation of crystalline RP, and finally the phosphorus@MWCNTs hybrids exhibited a significantly improved cycling stability.[20]

In addition to the synthesis techniques, the choice of carbon hosts is also of significant importance. Ideally, porous carbon hosts not only provide enough vacant space to confine RP, but also ameliorate electrical conductivity. So far, CNTs/MWCNTs,[5–9] graphene,[9–13] carbon nanofibers,[14,15] and some carbonaceous materials derived from biomass and organic precursors have been reported as porous carbon hosts for loading RP.[14–19] Among them, metal–organic frameworks (MOFs) derived porous carbons have attracted much interest due to their outstanding advantages such as controllable and high porosity, good thermal/chemical stability, high electrical conductivity, as well as easy modification with other elements and materials, etc.[21–24] Especially in the case of porous carbons derived from zinc-based MOFs, their porosity can be further increased by evaporating the reduced zinc at an operationally feasible boiling point, which would enable to load more RP to improve the mass loading and thus the corresponding energy density. Zeolitic imidazole framework (ZIF-8) is one of the most representative zinc-based MOFs, and its derived porous carbons have been utilized as carbon host for various active guests including P,[13,19] S,[25] SeS_2,[26] Te,[27] etc. using in high-performance lithium- and sodium-ion batteries. For instance, when confining nanoscale amorphous RP in the micropores of ZIF-8 derived carbon hosts via the conventional evaporation/condensation method, the obtained composites exhibited remarkably improved electrochemical performance.[19] However, due to the obvious limitations of the evaporation/condensation method itself, the undesirable deposition of crystalline RP on the outer surface and the concomitant formation of flammable white phosphors are difficult to be avoided, which would bring the potential issues of the cycling stability.

Herein, we demonstrate an improved solution-assisted encapsulation method to efficiently load phosphorus inside the pores of ZIF-8 derived carbon (ZIF-8-C) hosts at a mild temperature. Importantly, any pore smaller than 3 nm in ZIF-8-C is efficient for loading the polyphosphides anions (PP, mainly in the form of P_5^-). This method avoids the excess unreactive phosphorus being mingled with the final products and meanwhile eliminates the formation of harmful white phosphorous. What's more, phosphorus is successfully encapsulated into the micropores and mesopores of ZIF-8-C in PP form with a high phosphorous content of 30 wt%. Attributing to the excellent physical confinement of ZIF-8-C and incompletely filled pores that provide buffer space for volume expansion, the as-obtained ZIF-8-C@PP composites exhibit an improved capacity and long-termed cycling stability.

Figure 1a illustrates the preparation process of ZIF-8-C@PP. ZIF-8-C was synthesized as the carbon hosts via direct ZIF-8 carbonization at first. It is worth noting that ZIF-8 in this work was synthesized with an increased nanocrystal size to achieve the "golden size" of the final carbon hosts.[28–29] The as-synthesized ZIF-8 has a polyhedral morphology with active edges and

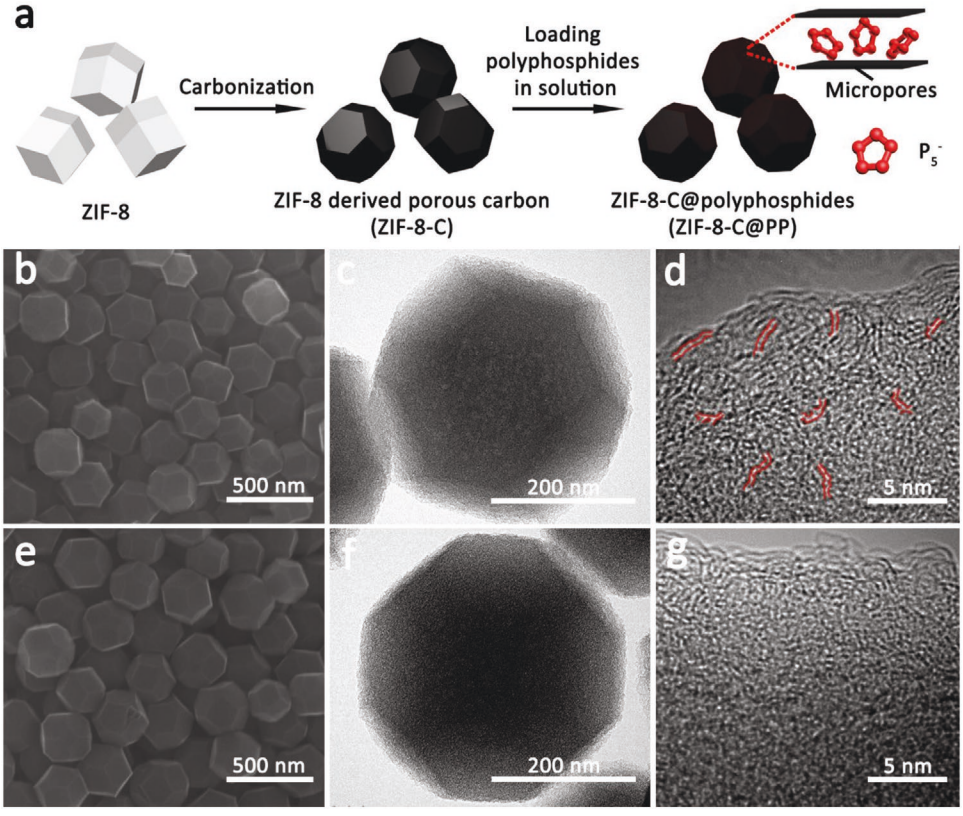

Figure 1. a) Schematic diagram of the preparation process of ZIF-8-C@PP; b) SEM, c) TEM, d) HRTEM images of ZIF-8-C; e) SEM, f) TEM, and g) HRTEM images of ZIF-8-C@PP.

apex angles (Figure S1, Supporting Information). After carbonization, ZIF-8-C was obtained with similar polyhedral morphology yet without obvious size reduction compared to ZIF-8 (Figure 1b), and the polyhedral morphology of ZIF-8-C was further confirmed by transmission electron microscope (TEM), as shown in Figure 1c. Intricate micropores of ZIF-8-C inherited from parent ZIF-8 crystal with a diameter of 0.3–0.4 nm can be seen clearly in high-resolution transmission electron microscope (HRTEM), partially marked with red dashed lines (Figure 1d). In order to feasibly encapsulate RP into nanopores of ZIF-8-C hosts, the nucleophile sodium ethoxide (NaOEt) was used to activate the decomposition of RP into PP (mainly including ring-shaped P_5^- anions as well as chain-shaped P_{16}^{2-} and P_{21}^{3-} anions) in solution under argon protection.[20,30] These soluble PP could readily diffuse into the pores of ZIF-8-C hosts through capillary phenomenon with the help of ultrasonic forces. In comparison to the conventional high-temperature evaporation/condensation method, the whole RP encapsulation process was conducted under a mild temperature (i.e., 80 °C), avoiding the conversion of RP to white phosphorus. Moreover, the absorbed PP anions on the surface of ZIF-8-C can be easily removed with common polar solvents (such as water and ethanol).[20]

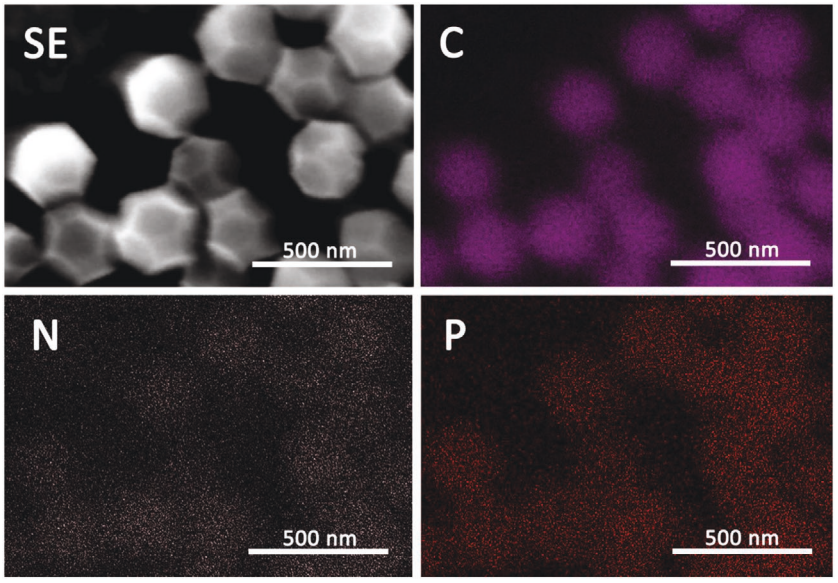

Figure 2. SEM image and corresponding EDX elemental mapping of carbon, nitrogen, phosphorus of ZIF-8-C@PP.

Figure 1e is the scanning electron microscope (SEM) image of the ZIF-8-C after the PP encapsulation (denoted as ZIF-8-C@PP). Obviously, there is almost no morphology change of ZIF-8-C@PP comparing to ZIF-8-C and no irregular bulk RP particles can be found on the surface of the final products. Furthermore, the TEM images of ZIF-8-C and ZIF-8-C@PP also show that they have similar polyhedral structures (Figure 1c–f). As for the HRTEM image of ZIF-8-C@PP, the contour of micropores near the edge of the particle is still clearly similar to that of ZIF-8-C, whereas they become blurred gradually with some explicit dark plaques visible inside. It suggests that the PP remained on the surface or even near the edges could be easily removed by common polar solvents and its form of existence is partial occupancy (Figure 1d–g). This form of phosphorus loading means the simultaneous presence of filled and unfilled portions in the micropores, resulting in a synergistic effect that the expansion of filled PP would be physically limited to a confined space while the unfilled part provides sufficient buffering space. The elemental distribution in ZIF-8-C@PP was characterized by energy-dispersive X-ray spectrometry (EDX) mapping (**Figure 2**). Usually, RP fragments are going to be found on the outer surface of ZIF-8-C if there are still some blocky RP not fully decomposed or retained PP agglomerated. Clearly, the EDX mapping further confirms the uniform distribution of phosphorus in ZIF-8-C@PP rather than speckle distribution, revealing the successful encapsulation of PP into the ZIF-8-C hosts. Moreover, the EDX mapping results also indicate that nitrogen atoms were doped into the carbon skeleton successfully during pyrolysis which will beneficial for improving the electrical conductivity of ZIF-8-C@PP.

Besides, the existence of intricate micropores and mesopores in ZIF-8-C and ZIF-8-C@PP were further verified with the nitrogen adsorption/desorption experiment. As shown in **Figure 3**a, the adsorption/desorption isotherm of ZIF-8-C is a typical H4 hysteresis loop with a composite of Types I and II adsorption division, which is normally found in carbon materials containing both micropores (<2 nm) and mesopores (>2 nm, <50 nm).[31] Enhanced absorbent-adsorptive interactions of narrow micropores with pore width less than 1 nm caused a cliffy uptake at low P/P_0 and larger mesopores would leave the hysteresis as a result of capillary condensation. The hierarchical micro-mesopores structure proved by adsorption/desorption isotherm can be well consistent with the result of the pore size distribution calculated by the density functional theory (DFT) method (Figure 3b). Ample micropores were inherited from the parent ZIF-8 and they have been demonstrated effectively prevent the agglomeration of nanosized RP inside.[19] Partial mesopores are probably produced during the reduction-evaporation process of zinc and also might be due to the measurement error caused by particle stacking. As can be seen in Figure 3a, ZIF-8-C@PP shows the alike isotherm, but with smaller adsorption and shrinking loop. The rapid decrease in the distribution of narrow micropores (<0.5 nm) indicates that the PP was loaded in micropores. Moreover, the Brunauer-Emmett–Teller (BET) specific surface area was decreased from 1535 $m^2\ g^{-1}$ of ZIF-8-C to 687 $m^2\ g^{-1}$ of ZIF-8-C@PP, and at the same time the pore volume reduced from 0.57 $m^3\ g^{-1}$ to 0.27 $m^3\ g^{-1}$ (in terms of pore width < 3 nm because the pore volume growth of ZIF-8-C@PP tends to be stable after 3 nm as well as ZIF-8-C, Figure 3b). Therefore, ZIF-8-C@PP still has a large specific surface area and a certain pore volume, unlike the results that the specific surface area and the pore volume drastically decreased using the conventional evaporation/condensation method. With solution-assisted encapsulation method, excess PP can be easily removed by water and

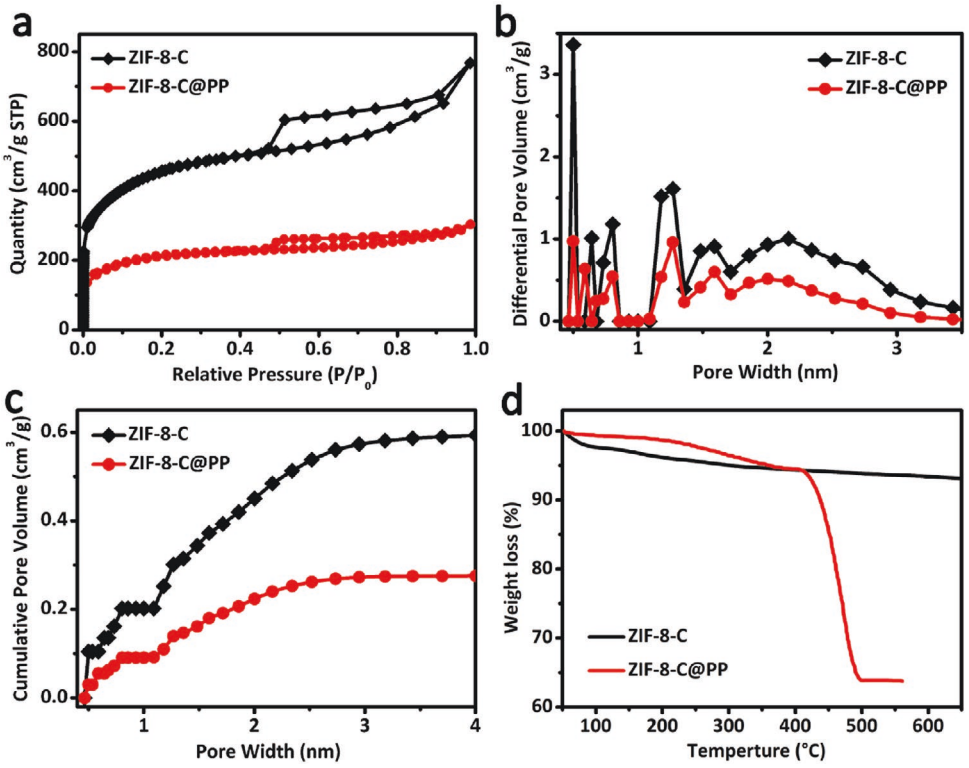

Figure 3. a) Nitrogen adsorption/desorption isotherm, b) pore size distribution and c) cumulative pore volume curves of ZIF-8-C and ZIF-8-C@PP. Pore size distribution and cumulative pore volume were investigated by the DFT method; d) TGA of ZIF-8-C and ZIF-8-C@PP.

ethanol rather than strongly adhering to the outer surface or blocking the pores. As a certain pore volume still exists in ZIF-8-C@PP, it can be inferred that there is only partial occupancy of phosphorus in the pores of ZIF-8-C hosts, which is in accordance with the HRTEM results. Those unfilled pores can buffer the volume expansion of phosphorus and also facilitate the electrolyte penetration. The content of phosphorus in the ZIF-8-C@PP was further determined by the thermogravimetric analysis (TGA) and it was calculated to reach 30 wt% (Figure 3d). According to the phosphorus density of 2.34 g cm^{-3}, the volume of 30 wt% of phosphorus in ZIF-8-C@PP (judging by the results of TGA, Figure 3d) divided by the volume of pore volume reduced in the corresponding system (judging by the results of nitrogen adsorption/desorption, Figure 3b) is 99.38%. This means that the amount of phosphorus in ZIF-8-C@PP and the amount of pore volume drop of ZIF-8-C@PP are perfectly matched, which means that it is the PP to actually enter the pores causing a matching pore volume drop.

X-ray diffraction (XRD) patterns and Raman spectra of ZIF-8-C, ZIF-8-C@PP, and commercial RP are compared in Figures S2a and S2b, Supporting Information, respectively. ZIF-8-C has three broad diffraction peaks at $2\theta \approx 14°$, 30°, and 43°, which represent the formation of graphitic carbon. The occurrence of some small sharp peaks arises from the increase in the number of planes during carbonization, as seen in SEM images. Commercial RP also shows three XRD diffraction peaks at $2\theta \approx 15°$, 31° and 55° and its Raman spectra have distinct characteristic peaks in the range of 300–500 cm^{-1}. As the results of phosphorus encapsulation, the peak intensity of the XRD characteristic peaks is significantly weakened. There are no obvious characteristic peaks of PP displayed in both XRD pattern and Raman spectra,[20] however, these results are the same as the confined amorphous RP in ZIF-8 derived carbon prepared by a vaporization-condensation-conversion method that reported previously.[19] The possible reason is that the signal of the substrate covers the signal of phosphorus. Furthermore, the composition of PP have been analyzed in detail via X-ray photoelectron spectroscopy (XPS) and the results are shown in Figures S2c–S2e, Supporting Information. The C1s spectrum of ZIF-8-C@PP indicates the existence of sp^2 carbon (284.7 eV), C = N/C—O (285.6 eV), C—N/C = O (288.5 eV), and O = C—O (289.6 eV).[27,32–35] For P2p, 129.5-130.6 eV is corresponding to phosphorus element, 133.1 eV may be derived from triethyl phosphite by-product,[20] 140.3 eV is related to zinc phosphide.[36] The presence of N-doping in the carbon skeleton comes from the ligand of parent ZIF-8 and a lot of studies have demonstrated N-doping in the carbon skeleton is capable of strengthening electrical activity and conductivity.[19,25,35]

The electrochemical performance of ZIF-8-C@PP was characterized by assembling half-cell LIBs with ZIF-8-C@PP as the anode and lithium metal as the counter electrode. It is worth noting that the MOF derived carbon-based electrode materials prefer to form a larger solid electrolyte interface (SEI) in the initial several cycles and the characteristic redox peaks in cyclic voltammetry (CV) curves tend to be stable with the progressive electrolyte wetting and penetration as the cycle continues.[19,23] The CV curves of ZIF-8-C@PP in this work were therefore collected after ten cycles activation. As shown in **Figure 4**a, the CV

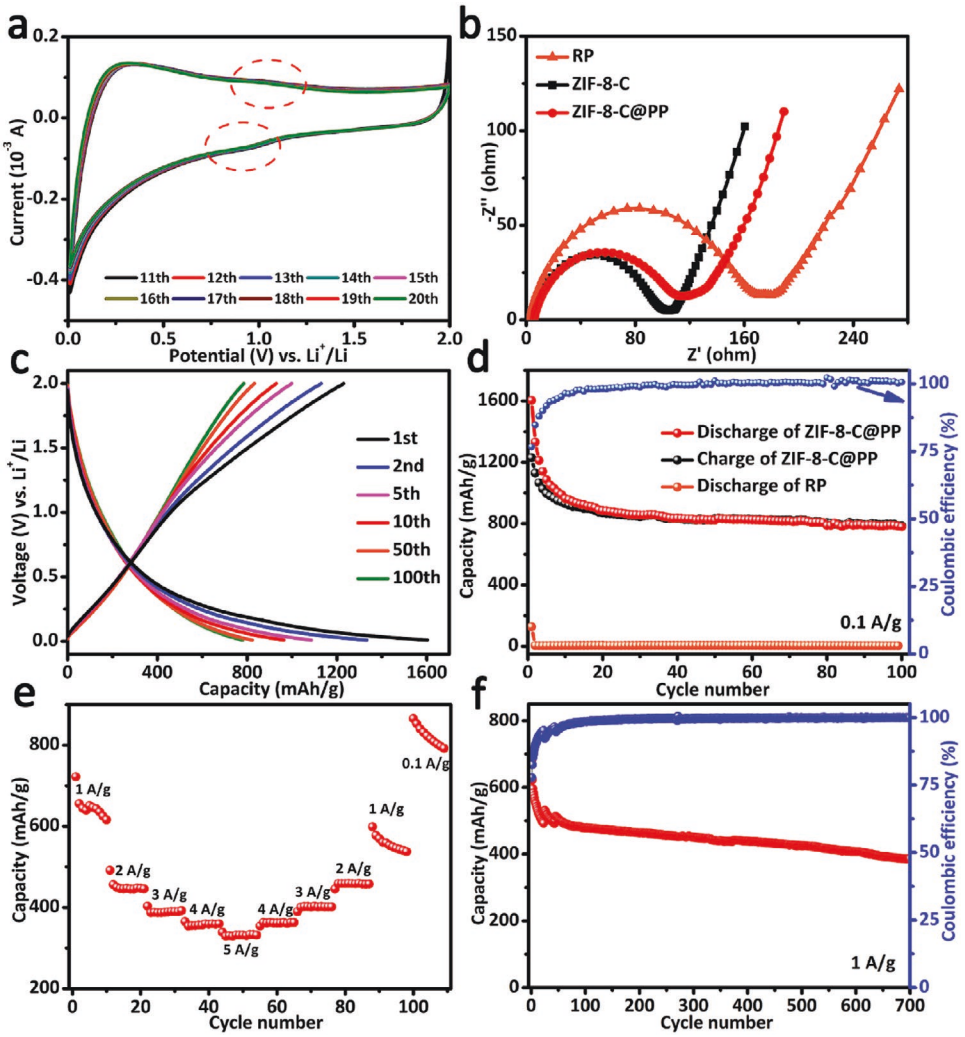

Figure 4. a) CV curves of ZIF-8-C@PP at 0.5 mV s^{-1} after ten cycles of activation; b) EIS of RP, ZIF-8-C, and ZIF-8-C@PP at open circuit potential; c) discharge and charge curves of ZIF-8-C@PP at 0.1 A g^{-1}; d) cycle performance curves of RP and of ZIF-8-C@PP at 0.1 A g^{-1}; e) Rate performance of ZIF-8-C@PP; f) discharge curve of ZIF-8-C@PP at 1 A g^{-1}.

measurement was carried out in a voltage range of 0.01 to 2 V versus Li^+/Li at a scan rate of 0.5 mV s^{-1}. All the CV curves between 11th and 20th cycles overlapped well, indicating the high reversible Li^+-storage capacity. The cathodic and anodic peaks at 0.96 and 1.03 V, respectively, in the CV curves can be detected, and they represented the Li-ion intercalation/deintercalation of P_5^- anion toward the ZIF-8-C@PP electrode. Since the P_5^- anion is the main form of PP in ZIF-8-C@PP, the delithiation peak is unimodal rather than multiple, for example, three or more peaks can usually be detected during the traditional conversion of the Li_xP phase to Li_yP intermediates ($1 \le y \le x \le 3$) and finally to P. The polarization curve (Figure 4c) of ZIF-8-C @ PP anode is also not typical for phosphorus anode materials because PP was obtained by chemical etching instead of physical evaporation-deposition.[7,17,20] Figure 4b shows the electrochemical impedance spectroscopy (EIS) of RP, ZIF-8-C, and ZIF-8-C@PP at an open circuit potential. All their Nyquist plot curves consist of a semicircle and a line from high frequency to low frequency, indicating that their electrochemical kinetics are subject to the control of both charge and mass transfer. As known, the diameter of the semicircle in the high frequency intuitively reflects the charge transfer resistance (R_{ct}). Benefiting from the conductive network provided by the porous carbon host in ZIF-8-C@PP, the R_{ct} of ZIF-8-C@PP electrode was greatly reduced compared to that of the conventional RP electrode, and thus would lead to a high rate performance of ZIF-8-C@PP.

The cycle performance of ZIF-8-C@PP anode at a low current density of 0.1 A g^{-1} is illustrated in Figure 4d. The first cycle has a high discharge capacity of 1603 mAh g^{-1} with a coulombic efficiency of about 76.7%. The irreversible capacity degradation during the beginning several cycles can be attributed to that the high specific surface area of MOF derived porous carbons requires the formation of a larger SEI,[19,23] which is in accordance with the CV measurement results. Even so, the Coulombic efficiency quickly raised and then stabilized at 100%, meanwhile the specific capacity finally maintained up to 786 mAh g^{-1} after 100 cycles.

Whereas, the RP electrode delivered the specific capacity being rapidly decayed to almost zero within ten cycles mainly due to its low conductivity (≈10^{-14} S m^{-1}) and huge volume expansion (>300%), indicating the unreliable cycling durability for the pure RP electrode (Figure 4d). Figures S4a and S4b, Supporting Information illustrate the discharge–charge curves and cycle performance curves of ZIF-8-C at 0.1 A g^{-1}, respectively. The specific capacity of ZIF-8-C maintained 186 mAh g^{-1} after 60 cycles. Owing to the high phosphorus content (i.e., 30 wt%) in ZIF-8-C@PP, the area-specific capacity of ZIF-8-C@PP anode reaches 754.6 µAh cm^{-2} at 0.1 A g^{-1}, which is much higher than that of P@N-MPC (162.7 µAh cm^{-2} at 0.15 A g^{-1} for sodium-ion battery anode) based on the vaporization-condensation-conversion method.[19] Figure 4e and Figure S3, Supporting Information display the rate performance and the current density was set from 1 A g^{-1} to 5 A g^{-1} and back to 0.1 A g^{-1} within 110 cycles. Intriguingly, as the current density returned back to 0.1 A g^{-1}, the specific capacity of 792 mAh g^{-1} was higher than 786 mAh g^{-1} remained after 100 continuous cycles at 0.1 A g^{-1}, revealing the high rate performance. Furthermore, the specific capacity attenuation was about 0.04% per cycle at 1 A g^{-1} within 700 cycles after ten cycles of activation, demonstrating the good cycling stability of ZIF-8-C@PP anode. (Figure 4f) Overall, the unique features of ZIF-8-C@PP may shed a bright future for large-scale energy storage due to its excellent battery performance:[37–46] first, ZIF-8-C@PP has a high phosphorous content of 30 wt% and nearly no crystalline RP formed on the outer surface attributing to the solution-based phosphorous encapsulation method thus enhancing the utilization of phosphorus and ensuring a large specific capacity for ZIF-8-C@PP; second, the pores in ZIF-8-C hosts physically confined the expansion of phosphorus and incompletely filled pores provided buffer space during volume expansion.

In summary, a facile solution-based phosphorus encapsulation method has been developed to address the tricky stability problem of phosphorus-based electrode materials. In this method, blocky RP was etched into nanosized PP to allow it to be feasibly incorporated into the pores of ZIF-8-C hosts in solution. ZIF-8-C@PP synthesized via this solution-based method efficiently circumvent the inevitable disadvantages of traditional evaporation-condensation method such as the formation of crystalline surface RP or white phosphorous and the high phosphorus encapsulation temperature. As a result, any pore less than 3 nm in ZIF-8-C is approved efficient for PP loading. Attributing to the elaborate structural design, ZIF-8-C@PP anode exhibits a high capacity, good cycling stability and high rate performance. This work demonstrates the generality of solution-based polyphosphides fabrication in carbon hosts and develops new avenues for the electrode materials design by using this mild-temperature solution-assisted phosphorus encapsulation strategy.

Experimental Section

Synthesis of ZIF-8-C: 0.735 g of $Zn(NO_3)_2{\cdot}6H_2O$ (99.0%, Shanghai Meixing Chemical Co., Ltd.) and dimethylimidazole (2-MeIM, 98%, Aladdin) were added to 70 mL of methanol in turn and stirred for 5 and 1 min, respectively. The molar ratio of Zn^{2+} to dimethylimidazole is 1:3. The solution reacted for 1 h. The white ZIF-8 precipitates was collected by centrifuging then drying at 80 °C for 12 h. In order to further synthesize ZIF-8-C, the finely ground white powder of ZIF-8 was pyrolyzed at 900 °C for 3 h under argon protection. The heating and cooling rate was controlled to be 5 °C min^{-1}. The black product was obtained and sonicated with 6 M HCl for 2 h. The final products were washed with distilled water then dried under vacuum.

Synthesis of ZIF-8-C@PP: All air sensitive reactions were performed under argon protection. After dissolving 110 mg of NaOEt (96%, Aladdin) in 3 mL of dimethyl sulfoxide (99%, Aladdin), 50 mg of ground RP (99.999%, Aladdin) was added to obtain a red-brown dispersion solution. Then, the mixture was heated up to 189 °C and kept refluxing for 6 h. As the reaction proceeds, the color of the solution turned into dark-purple, indicating the formation of polyphosphides anions. After that, 50 mg of previously synthesized ZIF-8-C was added to the collected supernatant that combined two RP etching reactions then sonicated for 2 h at 80 °C in order to enable the polyphosphides to fully enter the pores. The naturally cooled dispersion solution was washed and centrifuged by water and ethanol mixture. As-obtained product was dried overnight under vacuum.

Material Characterizations: SEM images were acquired by NOVA NANOSEM 200 at an accelerating voltage of 10 kV. TEM images were obtained from JEM-2100 (JEOL). The EDX spectrum was performed on Hitachi S-4800 with an EDX detector (Thermo Fisher Scientific). The nitrogen (N_2) adsorption/desorption data was recorded at 77 K using liquid nitrogen and analyzed by Micromeritics apparatus ASAP 2020M. TGA was obtained at Perkin-Elmer Pris-(TGA) Clarus SQ 8T with a heating rate of 10 °C min^{-1} under nitrogen flow. XRD patterns were obtained at the 2θ range of 10–80° on a Bruker D8 Advance diffractometer using Cu Kα radiation (λ = 0.15406 nm). XPS was performed on a spectrometer from Kratos Axis Ultradld using Mono Al Kα radiation at a power of 120 W (8 mA, 15 kV). Raman spectroscopy (JY-T64300, France) was tested with a laser excitation of 514 nm at ambient temperature. Micromeritics apparatus ASAP 2020M was used to characterize the porous structure of all samples, and it can directly calculate the DFT method related information based on the material's N_2 adsorption/desorption isotherm.

Electrochemical Tests: The electrochemical performance was characterized by using a 2025-type coin cell on the Neware Charge/Discharge apparatus. ZIF-8-C@PP (80 wt%), acetylene black (10 wt%) and poly(vinylidene fluoride) (10 wt%) were mixed to make a slurry, which was subsequently coated on the copper foil. After drying overnight at 60 °C under vacuum, it was sliced as the working electrode. The mass loading of each electrode was ≈4 mg cm^{-2}. The specific capacity was calculated per phosphorus only. Lithium metal acted as the counter electrode and reference electrode. The electrolyte was 1 M $LiPF_6$ in a 1:1 v/v mixture of ethylene carbonate (EC) and diethyl carbonate (DEC). The cells were assembled in an argon-filled glove box. For comparison, half-cell lithium-ion batteries with RP and ZIF-8-C as anodes, respectively, were also assembled and characterized under the same conditions. The mass loading of RP and ZIF-8-C anodes in the electrodes were 4 mg cm^{-2} and 1 mg cm^{-2}, respectively.

Supporting Information

Supporting Information is available from the Wiley Online Library or from the author.

Acknowledgements

The authors acknowledge funding from the National Natural Science Foundation of China (51972239 and 51872209), the Zhejiang Provincial Natural Science Foundation of China (LZ17E020002 and LZ20E010001), and German Research Foundation (DFG: LE2249/5-1). L.L. appreciates the China Scholarship Council (CSC) for providing a doctoral scholarship.

Conflict of Interest

The authors declare no conflict of interest.

Keywords

anodes, lithium-ion batteries, metal–organic framework derived carbon, physical confinement, red phosphorus

Received: December 6, 2019
Revised: January 28, 2020
Published online: February 21, 2020

[1] Y. Fu, Q. Wei, G. Zhang, S. Sun, *Adv. Energy Mater.* **2018**, *8*, 1703058.
[2] W. Liu, H. Zhi, X. Yu, *Energy Storage Mater.* **2019**, *16*, 290.
[3] Z. Li, H. Zhao, *J. Mater. Chem. A* **2018**, *6*, 24013.
[4] S. S. Zhang, *InfoMat* **2019**, https://doi.org/10.1002/inf2.12058.
[5] D. Zhao, J. Zhang, C. Fu, J. Huang, D. Xiao, M. M. F. Yuen, C. Niu, *J. Mater. Chem. A* **2018**, *6*, 2540.
[6] J. Zhang, D. Zhao, D. Xiao, C. Ma, H. Du, X. Li, L. Zhang, J. Huang, H. Huang, C. L. Jia, D. Tomanek, C. Niu, *Angew. Chem., Int. Ed.* **2017**, *56*, 1850.
[7] J. Xu, J. Ding, W. Zhu, X. Zhou, S. Ge, N. Yuan, *Sci. China Mater.* **2017**, *61*, 371.
[8] Y. Zhu, Y. Wen, X. Fan, T. Gao, F. Han, C. Luo, S. Lion, C. Wang, *ACS Nano* **2015**, *9*, 3254.
[9] J. Zhou, Z. Jiang, S. Niu, S. Zhu, J. Zhou, Y. Zhu, J. Liang, D. Han, K. Xu, L. Zhu, X. Liu, G. Wang, Y. Qian, *Chem* **2018**, *4*, 372.
[10] H. Gao, T. Zhou, Y. Zheng, Y. Liu, J. Chen, H. Liu, Z. Guo, *Adv. Energy Mater.* **2016**, *6*, 1601037.
[11] D. Zhao, B. Li, J. Zhang, X. Li, D. Xiao, C. Fu, L. Zhang, Z. Li, J. Li, D. Cao, C. Niu, *Nano Lett.* **2017**, *17*, 3376.
[12] Y. Liu, A. Zhang, C. Shen, Q. Liu, X. Cao, Y. Ma, L. Chen, C. Lau, T. C. Chen, F. Wei, C. Zhou, *ACS Nano* **2017**, *11*, 5530.
[13] Y. Wu, Z. Liu, X. Zhong, X. Cheng, Z. Fan, Y. Yu, *Small* **2018**, *14*, 1703472.
[14] X. Ma, L. Chen, X. Ren, G. Hou, L. Chen, L. Zhang, B. Liu, Q. Ai, L. Zhang, P. Si, J. Lou, J. Feng, L. Ci, *J. Mater. Chem. A* **2018**, *6*, 1574.
[15] B. Ruan, J. Wang, D. Shi, Y. Xu, S. Chou, H. Liu, J. Wang, *J. Mater. Chem. A* **2015**, *3*, 19011.
[16] Y. Sun, L. Wang, Y. Li, Y. Li, H. R. Lee, A. Pei, X. He, Y. Cui, *Joule* **2019**, *3*, 1080.
[17] W. Li, Z. Yang, M. Li, Y. Jiang, X. Wei, X. Zhong, L. Gu, Y. Yu, *Nano Lett.* **2016**, *16*, 1546.
[18] S. Yao, J. Cui, J. Huang, J.-Q. Huang, W. G. Chong, L. Qin, Y.-W. Mai, J.-K. Kim, *Adv. Energy Mater.* **2018**, *8*, 1702267.
[19] W. Li, S. Hu, X. Luo, Z. Li, X. Sun, M. Li, F. Liu, Y. Yu, *Adv. Mater.* **2017**, *29*, 1700253.
[20] J. Li, H. Jin, Y. Yuan, H. Lu, C. Su, D. Fan, Y. Li, J. Wang, J. Lu, S. Wang, *Nano Energy* **2019**, *58*, 23.
[21] X. Cao, C. Tan, M. Sindoro, H. Zhang, *Chem. Soc. Rev.* **2017**, *46*, 2660.
[22] Y. V. Kaneti, J. Tang, R. R. Salunkhe, X. Jiang, A. Yu, K. C. Wu, Y. Yamauchi, *Adv. Mater.* **2017**, *29*, 1700213.
[23] X. Zhang, A. Chen, M. Zhong, Z. Zhang, X. Zhang, Z. Zhou, X.-H. Bu, *Electrochem. Energy Rev.* **2018**, *2*, 29.
[24] X. C. Xie, K.-J. Huang, X. Wu, *J. Mater. Chem. A* **2018**, *6*, 6754.
[25] J. Zhang, M. Huang, B. Xi, K. Mi, A. Yuan, S. Xiong, *Adv. Energy Mater.* **2018**, *8*, 1701330.
[26] C. Liu, X. Huang, J. Wang, H. Song, Y. Yang, Y. Liu, J. Li, L. Wang, C. Yu, *Adv. Funct. Mater.* **2018**, *28*, 1705253.
[27] J. He, W. Lv, Y. Chen, K. Wen, C. Xu, W. Zhang, Y. Li, W. Qin, W. He, *ACS Nano* **2017**, *11*, 8144.
[28] L. Zhang, Z. Su, F. Jiang, L. Yang, J. Qian, Y. Zhou, W. Li, M. Hong, *Nanoscale* **2014**, *6*, 6590.
[29] J. Zhou, X. Yu, X. Fan, X. Wang, H. Li, Y. Zhang, W. Li, J. Zheng, B. Wang, X. Li, *J. Mater. Chem. A* **2015**, *3*, 8272.
[30] A. Dragulescu-Andrasi, L. Z. Miller, B. Chen, D. T. McQuade, M. Shatruk, *Angew. Chem., Int. Ed.* **2016**, *55*, 3904.
[31] M. Thommes, K. Kaneko, A. V. Neimark, J. P. Olivier, F. Rodriguez-Reinoso, J. Rouquerol, K. S. W. Sing, *Pure Appl. Chem.* **2015**, *87*, 1051.
[32] H. Liu, Y. Zou, L. Tao, Z. Ma, D. Liu, P. Zhou, H. Liu, S. Wang, *Small* **2017**, *13*, 1700758.
[33] H. X. Zhong, J. Wang, Y. W. Zhang, W. L. Xu, W. Xing, D. Xu, Y. F. Zhang, X. B. Zhang, *Angew. Chem., Int. Ed.* **2014**, *53*, 14235.
[34] Q. Zhao, L. Liu, R. Liu, L. Zhu, *Chem. Eng. J.* **2018**, *353*, 311.
[35] F. Zheng, Y. Yang, Q. Chen, *Nat. Commun.* **2014**, *5*, 5261.
[36] U. Elrod, M. Ch. Lux-Steiner, M. Obergfell, E. Bucher, L. Schlapbach, *Appl. Phys. B: Photophys. Laser Chem.* **1987**, *43*, 197.
[37] J. Wu, Y. Cao, H. Zhao, J. Mao, Z. Guo, *Carbon Energy* **2019**, *1*, 57.
[38] Y. Yuan, J. Lu, *Carbon Energy* **2019**, *1*, 8.
[39] Z. Yan, H. Jin, J. Guo, *Carbon Energy* **2019**, *1*, 246.
[40] X. Fan, X. Liu, W. Hu, C. Zhong, J. Lu, *InfoMat.* **2019**, *1*, 130.
[41] Y. X. Yao, X. Q. Zhang, B. Q. Li, C. Yan, P. Y. Chen, J. Q. Huang, Q. Zhang, *InfoMat.* **2019**, https://doi.org/10.1002/inf2.12046.
[42] B. Q. Li, L. Kong, C. X. Zhao, Q. Jin, X. Chen, H. J. Peng, J. L. Qin, J. X. Chen, H. Yuan, Q. Zhang, J. Q. Huang, *InfoMat.* **2019**, *1*, 533.
[43] Y. Zhao, Y. Zhu, X. Zhang, *InfoMat.* **2019**, https://doi.org/10.1002/inf2.12042.
[44] Z. Lin, Q. Xia, W. Wang, W. Li, S. Chou, *InfoMat.* **2019**, *1*, 376.
[45] D. Chen, H. Tan, X. Rui, Q. Zhang, Y. Feng, H. Geng, C. Li, S. Huang, Y. Yu, *InfoMat.* **2019**, *1*, 251.
[46] Y. Liang, C. Z. Zhao, H. Yuan, Y. Chen, W. Zhang, J. Q. Huang, D. Yu, Y. Liu, M. M. Titirici, Y. L. Chueh, H. Yu, Q. Zhang, *InfoMat.* **2019**, *1*, 6.